Phase Separation Behavior of Fe–Cr System Including α, α′, and σ Phases Using Phase-Field Modeling

Jeonghwan Lee[*1] and Kunok Chang[*2]

Department of Nuclear Engineering, Kyung Hee University, 17104, Republic of Korea

We suggested the multi-phase phase-field model of Fe–Cr system with consideration of not only α-α′ but also σ phase. In the prior phase-field study, one assumes the specific mechanism of phase separation, i.e., spinodal decomposition or nucleation and growth. On the other hand, our phase-field model can concurrently consider spinodal decomposition or nucleation/growth without any assumptions. With developed phase-field model of Fe–Cr system, we modelled three types of two-phase structures: α-α′, α-σ, α′-σ and single-phase σ region at T = 700 K and 1000 K.   [doi:10.2320/matertrans.MT-MB2022007]

1. Introduction

In various industry fields, the Fe–Cr alloy is widely used for structural materials due to its excellent corrosion resistance and high-temperature strength.[1–4] However, the phase separation can disrupt the integrity of structural material since it leads the embrittlement in Fe–Cr system.[1–6] Therefore, it is important to investigate the phase separation caused by the spinodal decomposition and the nucleation mechanisms in the Fe–Cr system.

In the Fe–Cr system, it coexists many different phases (α, α′, and σ) depending on the initial temperature and the initial Cr concentration.[2–15] Especially, the α′ phase is well-known to cause the phenomenon that hardening/embrittlement in the ferritic steel,[1–7,10] and the σ phase make the steel susceptible to localized corrosion.[12–15] Also, the misfit between α and α′ phases, which has body centered cubic (BCC) structure, is not significant due to the small lattice mismatch between Fe and Cr atoms, but the difference in crystal structure between α and σ phases affect the behavior of microstructural evolution.[5] Therefore, the comprehensive model considering both phase characteristics and crystal structure is necessary to understand the overall Fe–Cr system.

The α′ phase precipitation causes the embrittlement at less than 800 K in the Fe–Cr system.[2–11] Also, in the range from 800 K to 1100 K, the σ phase precipitation causes embrittlement.[11–15] To investigate the embrittlement phenomena, prior studies performed phase-field modeling assuming mechanisms such as spinodal decomposition or nucleation.[6,15–19] However, it is not enough to describe the phase separation initiation for σ phase, α and α′ phases.

In this study, we developed the phase field model that determines the phase separation of α, α′, and σ phases without assuming specific phase decomposition mechanisms. Unlike prior studies, our phase field model determines whether the spinodal decomposition or the nucleation occurs based on only initial Cr concentration and temperature.

To improve the computational efficiency and the numerical stability, we apply the acceleration methods of graphics processing unit (GPU) parallelization[16,20] and the semi-implicit Fourier spectral.[21–23]

2. CALPHAD Combined Phase-Field Method

2.1 Phase field model for multicomponent and multiphase system

To investigate the microstructural evolution in Fe–Cr system, we conduct the calculation of phase diagram (CALPHAD) based phase-field modeling. The governing equations are Cahn-Hilliard equation[24,25] and Allen-Cahn equation:[26]

$$\frac{\partial c(r,t)}{\partial t} = V_m^2 \nabla \cdot \left[M_{FeCr} \nabla \left(\frac{\delta F}{\delta c} \right) \right] \quad (1)$$

$$\frac{\partial \eta(r,t)}{\partial t} = -V_m L \left[\left(\frac{\delta F}{\delta \eta} \right) \right] \quad (2)$$

where $c(r,t)$ is the Cr concentration, V_m is the molar volume, $\eta(r,t)$ is the structural parameter, and L is the kinetic coefficient of $\eta(r,t)$. The $\frac{\delta F}{\delta c}$ and the $\frac{\delta F}{\delta \eta}$ are functional derivatives of the Cr concentration ($c(r,t)$) and the structural parameter ($\eta(r,t)$). The M_{FeCr} is the mobility given by Darken's equation:[16,27,28]

$$M_{FeCr} = \frac{1}{V_m} [cM_{Fe} + (1-c)M_{Cr}]c(1-c) \quad (3)$$

where M_{Fe} and M_{Cr} are atomic mobility of the Fe and Cr atoms, it can calculate through Einstein's relation $M_A = D_A/RT$. D_A is the diffusion coefficient of A atom, R is the gas constant and T is the absolute temperature, and D_{Fe} and D_{Cr} given by[18]

$$D_{Fe} = 1.0 \times 10^{-4} \, exp\left(-\frac{294 \, (\text{kJ/mol})}{RT} \right) \quad (4)$$

$$D_{Cr} = 2.0 \times 10^{-5} \, exp\left(-\frac{308 \, (\text{kJ/mol})}{RT} \right) \quad (5)$$

The total free energy of Fe–Cr system can be expressed as[16,29]

[*1]Graduate Student, Kyung Hee University
[*2]Corresponding author, E-mail: kunok.chang@khu.ac.kr

$$F(r, t) = \int_V \left\{ \frac{1}{V_m} \left[\begin{array}{c} (1 - h(\eta))f^{BCC}(c) + h(\eta)f^{\sigma}(c) \\ + \frac{W}{2}\eta^2(1 - \eta)^2 + \frac{1}{2}\kappa_c(\nabla c)^2 + \frac{1}{2}\kappa_\eta(\nabla\eta)^2 \end{array} \right] \right\} dV \qquad (6)$$

where $h(\eta)$ is a polynomial function $h(\eta) = \eta^3(6\eta^2 - 15\eta + 10)$, W is the height of the double well potential, κ_c and κ_η are the gradient energy coefficient of $c(r, t)$ and $\eta(r, t)$, respectively. If the structural order parameter (η) becomes 0, then the polynomial function for diffused interface ($h(\eta)$) becomes 0, so the contribution of the free energy for the sigma phase to the bulk driving force becomes 0. On the other hand, if the structural order parameter (η) becomes 1, the free energy for sigma phase is dominant the bulk driving force. We considered the regular solution model and the two sublattice model to calculate the molar free energies of BCC phase ($f^{BCC}(c)$) and sigma phase ($f^{\sigma}(c)$) in Fe–Cr binary system.[14,17,30]

$$f^{BCC}(c) = (1 - c)G^0_{Fe} + cG^0_{Cr} + L_{FeCr}c(1 - c)$$
$$+ RT(c \ln c + (1 - c)\ln(1 - c)) \qquad (7)$$

$$f^{\sigma}(c) = y_{Fe}G^{0,\sigma}_{Fe} + y_{Cr}G^{0,\sigma}_{Cr} + G^{ideal}_{FeCr} + G^{Excess}_{FeCr} \qquad (8)$$

where y_{Fe} and y_{Cr} are the lattice fraction of Fe and Cr component, $G^{0,\sigma}_{Fe}$ and $G^{0,\sigma}_{Cr}$ are the free energies when only one pure element is included, G^0_{Fe} and G^0_{Cr} are the molar free energies for pure elemental Fe and Cr, respectively. The L_{FeCr} is the interaction parameter between Fe and Cr atoms, G^{ideal}_{FeCr} and G^{Excess}_{FeCr} are the free energies for ideal mixing and excess terms, respectively.

2.2 Governing equation applied semi-implicit Fourier spectral method

To improve the numerical stability, we applied semi-implicit Fourier spectral method to Cahn Hilliard equation in eq. (1) and Allen Cahn equation in eq. (2), then rearranged eq. (1) and (2) as[21,22]

$$\frac{\partial c(\mathbf{r}, t)}{\partial t} = V_m \nabla \cdot \left[M_{FeCr} \nabla \left(\begin{array}{c} (1 - h(\eta))\frac{\partial f^{BCC}(c)}{\partial c} + h(\eta)\frac{\partial f^{\sigma}(c)}{\partial c} \\ -\kappa_c\nabla^2 c(\mathbf{r}, t) \end{array} \right) \right] \qquad (9)$$

$$\frac{\partial \eta(\mathbf{r}, t)}{\partial t} = -L \left[\begin{array}{c} -\frac{\partial h(\eta)}{\partial \eta}f^{BCC}(c) + \frac{\partial h(\eta)}{\partial \eta}f^{\sigma}(c) \\ +W\eta(1 - 2\eta)(1 - \eta) - \kappa_\eta\nabla^2\eta \end{array} \right] \qquad (10)$$

The eq. (9) and eq. (10) are approximated using the semi-implicit Fourier spectral method as follows:

$$\tilde{c}^{n+1}(\mathbf{k}, t) - \tilde{c}^n(\mathbf{k}, t) = \frac{V_m\Delta t i\mathbf{k} \cdot \left\{ M_{FeCr} \times \left[i\mathbf{k}' \left(\left\{ \begin{array}{c} (1 - h(\eta^n))\frac{\partial f^{BCC}(c)}{\partial c} \\ +h(\eta^n)\frac{\partial f^{\sigma}(c)}{\partial c} \end{array} \right\}^n_{\mathbf{k}'} + \kappa_c\mathbf{k}'^2\tilde{c}^n(\mathbf{k}, t) \right) \right]_{\mathbf{r}} \right\}_{\mathbf{k}}}{(1 + S_c\Delta t\kappa_c\mathbf{k}^4)} \qquad (11)$$

$$\tilde{\eta}^{n+1}(\mathbf{k}, t) = \frac{\left(\tilde{\eta}^n(\mathbf{k}, t) - \Delta t L \left\{ -\frac{\partial h(\eta)}{\partial \eta}f^{BCC}(c) + \frac{\partial h(\eta)}{\partial \eta}f^{\sigma}(c) + W\eta(1 - 2\eta)(1 - \eta) \right\}^n_{\mathbf{k}} \right)}{(1 + \Delta t L\kappa_\eta\mathbf{k}^2)} \qquad (12)$$

where $\mathbf{k} = (k_1, k_2)$ is the reciprocal vector in the Fourier space. The $\tilde{c}^n(\mathbf{k}, t)$ and the $\tilde{\eta}^n(\mathbf{k}, t)$ are the Fourier transforms of $c(\mathbf{r}, t)$ and $\eta(\mathbf{r}, t)$. The S_c is the hypothetical mobility parameter defined as $S_c = \frac{1}{2}[\max(M_{FeCr}) + \min(M_{FeCr})]$ where the $\max(M_{FeCr})$ and the $\min(M_{FeCr})$ are maximum and minimum values of M_{FeCr}.[21]

2.3 Computational details

We used dimensionless values to simulate the behavior of precipitation in Fe–Cr system. The normalized values are $\mathbf{r}^* = \mathbf{r}/l$, $\nabla^* = \partial/\partial(\mathbf{r}/l)$, $t^* = tD/l^2$, $M^* = RT^*M_{FeCr}/D$, $f^{BCC^*}(c) = f^{BCC}(c)/RT^*$, $f^{\sigma^*}(c) = f^{\sigma}(c)/RT^*$, and $\kappa^*_c = \kappa/(RT^*l^2)$ with $D = D_{Cr}$, $T^* = 900$ K, and $l = 2.856$ Å. The kinetic coefficient $L = 1$, the height of the double well potential $W = 1$, the gradient energy coefficients are $\kappa_c = \frac{1}{6}l^2L_{FeCr}$ and $\kappa_\eta = 1$. The initial fluctuation for Cr concentration is range of $-0.005 \sim 0.005$. The time step

was $\Delta t^* = 0.001$ and the simulation cell size was $1024\Delta x^* \times 1024\Delta y^*$ (292.45 nm $\times$ 292.45 nm), wherein the $\Delta x^* = 1.0$.

To improve the computational efficiency, we applied parallelization technique using compute unified device architecture (CUDA) to conduct the Fourier transform process and calculation of free energies.[16,20,31]

In the Fig. 1 that phase diagram of Fe–Cr system using FactSage thermochemical software,[32] there are various phases existing with α, α', and σ phases as the composition and the temperature.

When conducting the phase-field simulation, we seeded the structure parameter (η) in a spherical shape with a radius of $5\Delta x^*$, and the number of seeds was 100. Especially, the initial state of η is the same in all cases. It means that we performed phase-field modeling by changing only the temperature and the initial Cr concentration.
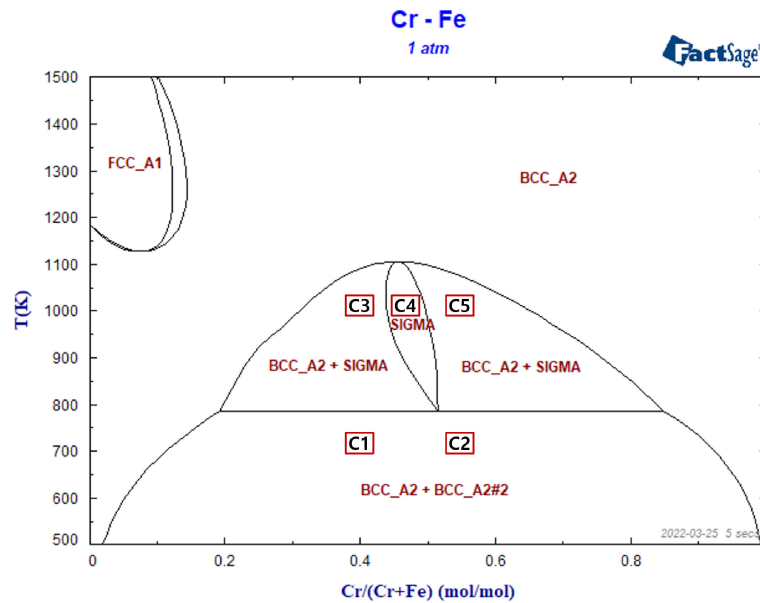
Fig. 1   The phase diagram of Fe–Cr system using FactSage thermochemical software where temperature range of 500 K to 1500 K.

Table 1   Five sets of simulation for various composition, existing phases, and system temperature.

Case	Temperature	Composition	Existing phases
C1	700 K	Fe-40Cr	α, α'
C2	700 K	Fe-55Cr	α, α'
C3	1000 K	Fe-40Cr	α, σ
C4	1000 K	Fe-45Cr	σ
C5	1000 K	Fe-55Cr	σ, α'

3.   Simulation Results and Discussion

We observed the behavior of microstructural evolution for α, α' and sigma phases at 700 K and 1000 K. To investigate the phase separation behavior of Fe–Cr system, we performed five sets of simulations shown in Table 1.

3.1   The phase separation behaviors in Fe–Cr system at 700 K

As shown in Fig. 2, when average Cr concentration was 40 at%, the phase separation occurred through spinodal decomposition mechanism. Also, during the phase separation, the average α' precipitate size increased due to the coarsening kinetics. Moreover, the Cr concentration of precipitate phase and matrix phase were around 90 at% and 10 at%, which are almost same to equilibrium concentration in phase diagram of Fe–Cr system at 700 K.

The maximum value for structural parameter (η) is 1 at initial state. However, it is decreased over time and becomes zero around $t^* = 7.5 \times 10^3$ in Fig. 3. Therefore, only free energy for BCC phases affects the total free energy in cases (C1) and (C2), and only α and α' phases exist at 700 K due to they are stable in Fig. 1.

When average Cr concentration is 55 at%, the average α' precipitate size increase over time. It is same to when Cr concentration is 40 at%. However, we observed that more
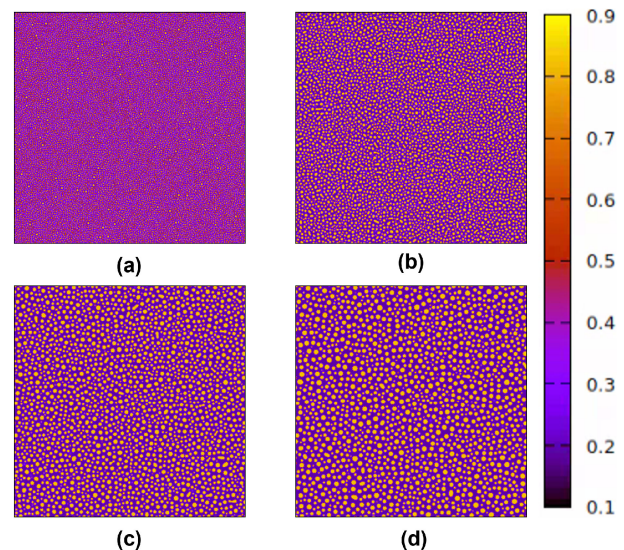

Fig. 2   When Cr concentration was 40 at%, the morphological variation for precipitate over time at 700 K: (a) $t^* = 1.0 \times 10^4$, (b) $t^* = 1.0 \times 10^5$, (c) $t^* = 5.0 \times 10^5$, (d) $t^* = 1.0 \times 10^6$.

interconnected microstructure for α' precipitate when Cr concentration is 55 at% in Fig. 4.

We observed the microstructure morphological variation through the spinodal decomposition and subsequent coarsening, it is consistent with formal studies.[15–17]

3.2   The phase separation behaviors in Fe–Cr system at 1000 K

According to Fig. 1, the Fe–Cr system has two phases at 1000 K, the phases in the area (C3) separated into the σ phase and α phase. Likewise, the phases in the area (C5) separated into the σ phase and α' phase. Our phase field modeling results in Fig. 5 are consistent with phase diagram of Fe–Cr system.

At 1000 K, the sum of structural parameter increases as shown in Fig. 6. Also, the η more interconnected over time,
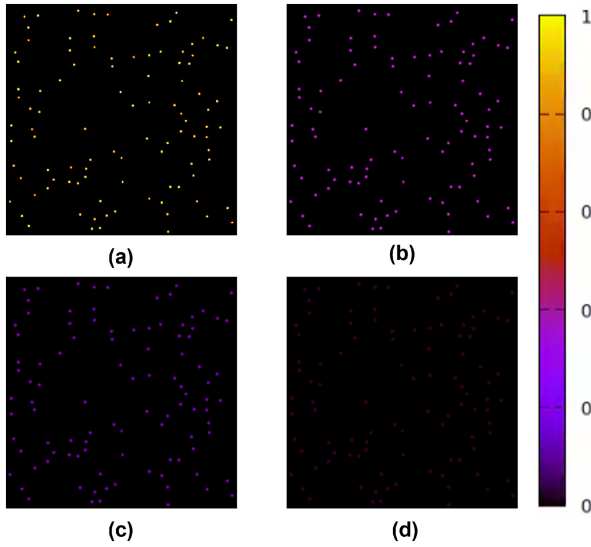
Fig. 3 The variation for structural parameter (η) over time when Cr concentration was 40 at% at 700 K: (a) $t^* = 0$, (b) $t^* = 2.5 \times 10^3$, (c) $t^* = 5.0 \times 10^3$, (d) $t^* = 7.5 \times 10^3$.
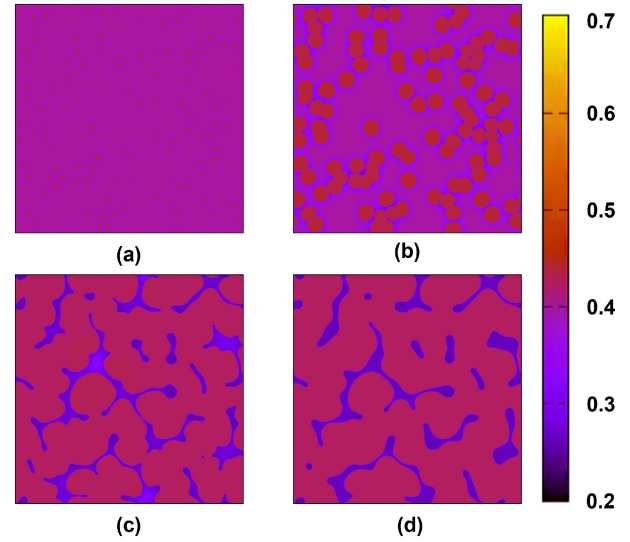

Fig. 5 When Cr concentration was 40 at%, the morphological variation for precipitate over time: (a) $t^* = 1.0 \times 10^4$, (b) $t^* = 1.0 \times 10^5$, (c) $t^* = 5.0 \times 10^5$, (d) $t^* = 1.0 \times 10^6$.
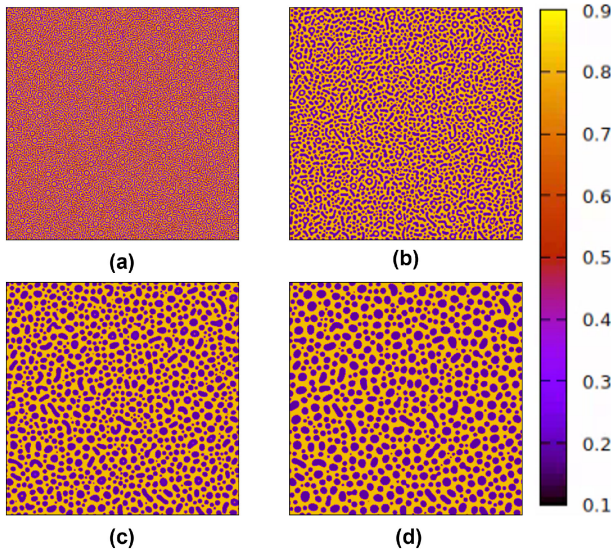

Fig. 4 When Cr concentration was 55 at%, the morphological variation for precipitate over time at 700 K: (a) $t^* = 1.0 \times 10^4$, (b) $t^* = 1.0 \times 10^5$, (c) $t^* = 5.0 \times 10^5$, (d) $t^* = 1.0 \times 10^6$.
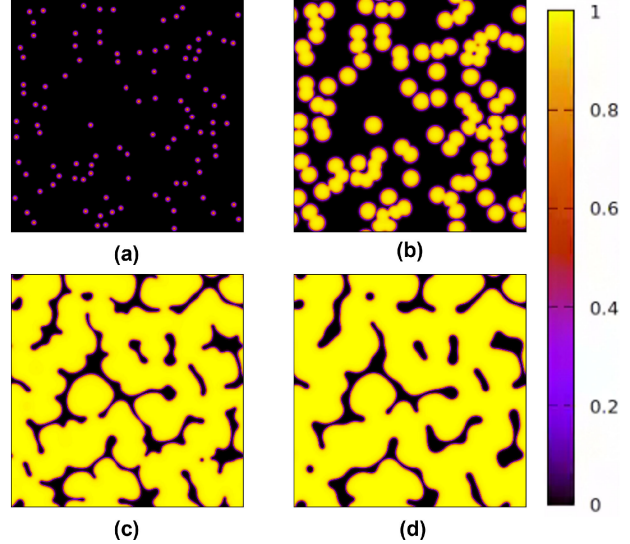

Fig. 6 The variation for structural parameter (η) over time when Cr concentration was 40 at% at 1000 K: (a) $t^* = 1.0 \times 10^4$, (b) $t^* = 1.0 \times 10^5$, (c) $t^* = 5.0 \times 10^5$, (d) $t^* = 1.0 \times 10^6$.

and the Cr concentration field follows the structural parameter.

When average Cr concentration is 55 at%, the Cr concentration separate into 45 at% and 70 at% at $t^* = 1.0 \times 10^6$ as shown in Fig. 7. Also, the Cr concentration is 70 at% when the structural parameter is zero, and the Cr concentration is 45 at% when structural parameter is 1.

In Fig. 1, when the average Cr concentration is 45 at%, there is a sigma single phase at 1000 K. Our modeling result that the phase separation does not occur when the average Cr concentration is 45 at% (C4), is consistent with the phase diagram in the Fe–Cr system.

Our simulation results that equilibrium concentration (c^{eq}), volume fraction using phase-field simulation (V_f^{PFM}), theoretical volume fraction using equilibrium concentration ($V_f^{c^{eq}}$), and percentage error ($|(V_f^{PFM} - V_f^{c^{eq}})/V_f^{c^{eq}}|$) are shown

in Table 2. Due to it reaching the equilibrium state, there is a difference between V_f^{PFM} and $V_f^{c^{eq}}$, and the $|(V_f^{PFM} - V_f^{c^{eq}})/V_f^{c^{eq}}|$ is less than 5%.

As shown in Fig. 8, there is a range of Cr concentration where the molar free energy of σ phase is lower than the free energy of α and α' phases at 1000 K. Therefore, depending on the initial Cr concentration, the precipitation for sigma phase can occur, and our simulation results are consistent with these thermodynamic results.

4. Conclusion and Future Work

In the Fe–Cr system, we conducted the phase-field modeling that comprehensively considered spinodal decomposition and nucleation without prior assumption for the phase separation mechanism. We observed the four cases of microstructure of α and α' phases, α and σ phases, σ single
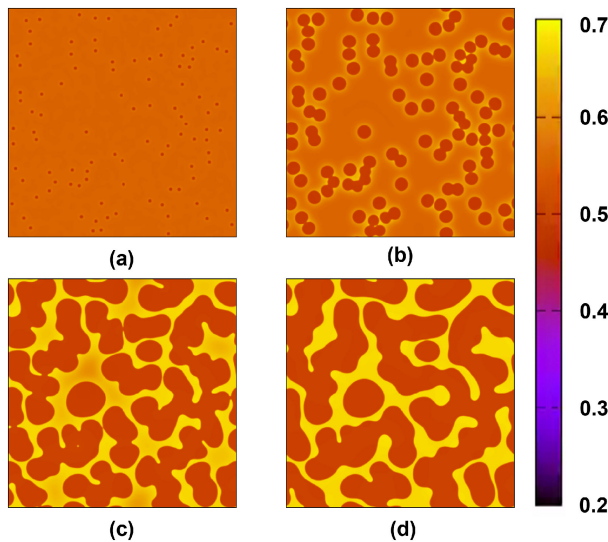
Fig. 7 When Cr concentration was 55 at%, the morphological variation for precipitate over time: (a) $t^* = 1.0 \times 10^4$, (b) $t^* = 1.0 \times 10^5$, (c) $t^* = 5.0 \times 10^5$, (d) $t^* = 1.0 \times 10^6$.

Table 2 The equilibrium concentration (c^{eq}), volume fraction using phase-field modeling (V_f^{PFM}), theoretical volume fraction using equilibrium concentration ($V_f^{c^{eq}}$), and percentage error ($|(V_f^{PFM} - V_f^{c^{eq}})/V_f^{c^{eq}}|$) at $t^* = 1.0 \times 10^6$.

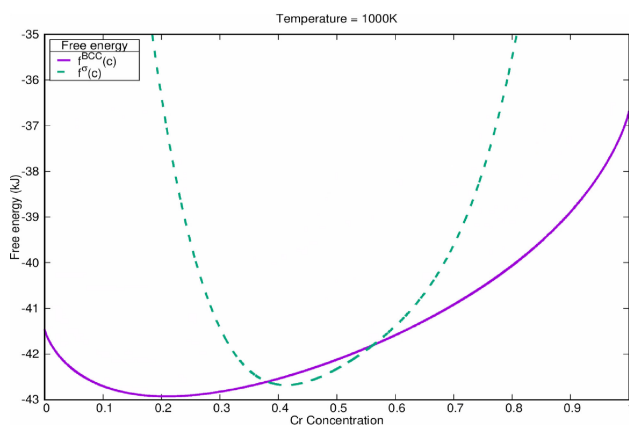| Case	c^{eq}	V_f^{PFM}	$V_f^{c^{eq}}$	$\left\| \dfrac{V_f^{c^{eq}} - V_f^{PFM}}{V_f^{c^{eq}}} \right\|$
C1	0.182, 0.827	0.337	0.330	2.1%
C2	0.172, 0.820	0.585	0.583	0.3%
C3	0.250, 0.425	0.856	0.839	2.0%
C4	0.498, 0.682	0.719	0.691	4.0%
C5	0.45	1.0	1.0	0

Fig. 8 The molar free energies for BCC phase and Sigma phase at 1000 K.

phase, and α' and σ phases based on thermodynamically determined Cr composition and temperature. The microstructure characteristics were evaluated using our phase-field model, and it was consistent with the phase diagram of Fe–Cr. However, in this study, we didn't consider the precipitates size and the microstructural evolution kinetics for the sigma phase. Also, elastic effect due to the lattice mismatch between the three phases (α, α' and σ) cannot be ignored. So, the thermodynamic properties of the sigma phase and the elastic effect between the phases will be studied in the future.

Acknowledgments

REFERENCES

1) M.K. Miller, J.M. Hyde, M.G. Hetherington, A. Cerezo, G.D.W. Smith and C.M. Elliott: Acta Metall. Mater. **43** (1995) 3385–3401.
2) P.J. Grobner: Metall. Trans. **4** (1973) 251–260.
3) D. Chandra and L.H. Schwartz: Metall. Trans. **2** (1971) 511–519.
4) H.D. Solomon and L.M. Levinson: Acta Metall. **26** (1978) 429–442.
5) Y.S. Li, S.X. Li and T.Y. Zhang: J. Nucl. Mater. **395** (2009) 120–130.
6) P. Hedström, S. Baghsheikhi, P. Liu and J. Odqvist: Mater. Sci. Eng. A **534** (2012) 552–556.
7) G. Bonny, D. Terentyev and L. Malerba: Scr. Mater. **59** (2008) 1193–1196.
8) W. Xiong, M. Selleby, Q. Chen, J. Odqvist and Y. Du: Crit. Rev. Solid State Mater. Sci. **35** (2010) 125–152.
9) J. Vreštzál, J. Houserová and M. Šob: J. Min. Metall. B **38** (2002) 205–211.
10) O. Soriano-Vargas, E.O. Avila-Davila, V.M. Lopez-Hirata, H.J. Dorantes-Rosales and J.L. Gonzalez-Velazquez: Mater. Trans. **50** (2009) 1753–1757.
11) C. Ying-Yu, L. Jen-Chwen and Y.A. Chang: Calphad **11** (1987) 57–72.
12) Y. Zhang, Z. Liu and D. Li: Mater. Trans. **62** (2021) 756–762.
13) M.H. Lewis: Acta Metall. **14** (1966) 1421–1428.
14) J. Houserová, M. Friák, M. Šob and J. Vřešt'ál: Comput. Mater. Sci. **25** (2002) 562–569.
15) A. Malik, J. Odqvist, L. Höglund, S. Hertzman and J. Ågren: Metall. Mater. Trans. A **48** (2017) 4914–4928.
16) Y.S. Li, H. Zhu, L. Zhang and X.L. Cheng: J. Nucl. Mater. **429** (2012) 13–18.
17) J. Lee and K. Chang: Comput. Mater. Sci. **169** (2019) 109088.
18) W. Liu, Y. Li, X. Wu, Z. Hou and K. Hu: J. Mater. Eng. Perform. **25** (2016) 1924–1930.
19) L. Zhu, Y. Li, C. Liu, S. Chen, S. Shi and S. Jin: Model. Simul. Mater. Sci. Eng. **26** (2018) 035015.
20) Nvidia CUDA, Programming guide (2011).
21) J. Zhu, L.Q. Chen, J. Shen and V. Tikare: Phys. Rev. E **60** (1999) 3564.
22) L.Q. Chen and J. Shen: Comput. Phys. Commun. **108** (1998) 147–158.
23) D. Li, Z. Qiao and T. Tang: SIAM J. Numer. Anal. **54** (2016) 1653–1681.
24) J.W. Cahn: Acta Metall. **9** (1961) 795–801.
25) J.W. Cahn and J.E. Hilliard: J. Chem. Phys. **28** (1958) 258–267.
26) S.M. Allen and J.W. Cahn: Acta Metall. **27** (1979) 1085–1095.
27) J.O. Andersson and J. Ågren: J. Appl. Phys. **72** (1992) 1350–1355.
28) R.R. Mohanty, J.E. Guyer and Y.H. Sohn: J. Appl. Phys. **106** (2009) 034912.
29) W. Shin and K. Chang: Comput. Mater. Sci. **182** (2020) 109775.
30) J.O. Andersson and B. Sundman: Calphad **11** (1987) 83–92.
31) J. Lee, K. Park and K. Chang: Metals **11** (2020) 4.
32) C.W. Bale, P. Chartrand, S.A. Degterov, G. Eriksson, K. Hack, R.B. Mahfoud, J. Melançon, A.D. Pelton and S. Petersen: Calphad **26** (2002) 189–228.